


 Cite this: *Nanoscale*, 2021, **13**, 14081

Observation of robust charge transfer under strain engineering in two-dimensional MoS₂-WSe₂ heterostructures†

 Shu-Wen Zheng,^a Hai-Yu Wang,^{id} *^a Lei Wang,^{id} *^a Yang Luo,^b Bing-Rong Gao^a and Hong-Bo Sun^{id} ^c

Strain is one of the effective ways to modulate the band structure of monolayer transition metal dichalcogenides (TMDCs), which has been reported in theoretical and steady-state spectroscopic studies. However, the strain effects on the charge transfer processes in TMDC heterostructures have not been experimentally addressed thus far. Here, we systematically investigate the strain-mediated transient spectral evolutions corresponding to excitons at band-edge and higher energy states for monolayer MoS₂ and monolayer WSe₂. It is demonstrated that Γ and K valleys in monolayer WSe₂ and monolayer MoS₂ present different strain responses, according to the broadband femtosecond pump-probe experimental results. It is further observed that the resulting band offset changes tuned by applied tensile strains in MoS₂-WSe₂ heterostructures would not affect the band-edge electron transfer profiles, where only monolayer WSe₂ is excited. From a flexible optoelectronic applications perspective, the robust charge transfer under strain engineering in TMDC heterostructures is very advantageous.

Received 31st March 2021

Accepted 19th July 2021

DOI: 10.1039/d1nr02014e

rsc.li/nanoscale

Introduction

As an emerging class of two-dimensional (2D) semiconductors, monolayer transition metal dichalcogenides (TMDCs) with broken inversion symmetry have a series of fascinating features, for example, exhibiting direct bandgaps, unlike the few-layer indirect-bandgaps and bulk counterparts, and are further affected by the quantum confinement effect, valley selection optical effects, and many-body effects.^{1–5} Therefore, TMDCs are not only used in basic studies on condensed matter physics but also applied in the preparation of electronic and optoelectronic devices.^{6–10} The unique symmetry and tunable bandgap of monolayer TMDCs also make their optical and electronic properties change greatly when lower strains are applied, compared with that of graphene.^{11,12} It is reported that the zero bandgap of graphenes could open up at a shear strain of $\sim 16\%$, and reach a maximum value of 0.72 eV at a shear strain of 20%.¹³

The typical size of bandgap change of TMDCs in response to strains is also at tens meV% strain.¹⁴ As a result, it could realize more functionality in TMDC-based flexible devices.^{15–18}

So far, massive efforts have been spent on the strain engineering of monolayer TMDCs.^{19–22} Bolotin *et al.* have employed Raman and photoluminescence (PL) spectroscopy techniques to estimate the strain-induced band structure changes of the monolayer and bilayer MoS₂.¹⁴ Desai *et al.* have demonstrated a drastically increased PL intensity in strained few-layer WSe₂, which could be attributed to the transition from indirect bandgap to direct bandgap.²³ In addition to steady-state experiments, there are also theoretical simulations about the strain effects on monolayer TMDCs. According to the *ab initio* simulation, Priya Johari *et al.* have shown that the bandgaps of TMDCs could be tuned by applying strains, which are more sensitive to tensile and shear strain than that for graphene.²⁴ Ashok Kumar *et al.* have calculated the influence of uniaxial and biaxial strains on electronic and dielectric properties of MoX₂ (X = S, Se, Te) by the first principle calculations.²⁵ Yang *et al.* have simulated the strain effects on the charge carrier lifetimes in monolayer WSe₂ by *ab initio* time-domain analysis.²⁶ Due to the lattice mismatch and the interlayer interaction, it is expected that 2D heterostructures also could be strongly affected by strain. Pak *et al.* have investigated the strain-dependent phonon energy and exciton emission in MoS₂-WS₂ heterostructures by Raman and PL spectroscopy techniques, too.²⁷ However, strain effects on the interfacial

^aState Key Laboratory of Integrated Optoelectronics, College of Electronic Science and Engineering, Jilin University, 2699 Qianjin Street, Changchun 130012, China. E-mail: haiyu_wang@jlu.edu.cn

^bChangchun Institute of Optics, Fine Mechanics and Physics, Chinese Academy of Sciences, Changchun 130033, China

^cState Key Laboratory of Precision Measurement Technology and Instruments, Department of Precision Instrument, Tsinghua University, Haidian, Beijing 100084, China

†Electronic supplementary information (ESI) available. See DOI: 10.1039/d1nr02014e

charge transfer processes in TMDC heterostructures have not been experimentally addressed yet.

Here, we have applied a series of (0.4%, 0.8%, 1.2%) strains to monolayer MoS₂ (WSe₂) and MoS₂-WSe₂ heterostructures on polyethylene terephthalate (PET) flexible substrates (1 cm × 1 cm), and investigated their steady-state optical properties and time-resolved excited-state processes. When the mechanical tensile strain applied to the monolayer MoS₂ and WSe₂ increases from 0% to 1.2%, the bandgap at K point shrinks 41 meV and 16 meV for monolayers of MoS₂ and WSe₂, respectively, according to the redshift of A-exciton bleaching peak measured by broadband transient absorption (TA) spectroscopy. It was further found that the band offset changes for MoS₂-WSe₂ heterostructure under those tensile strains would not affect the band-edge electron transfer profiles in the case that only monolayer WSe₂ is excited. Our investigation suggests that TMDC heterostructures could be promising candidates for flexible applications.

Experimental

Sample preparation

MoS₂ and WSe₂ monolayer continuous films were purchased from 6 Carbon Technology, Shenzhen. The MoS₂ (WSe₂) film made by chemical vapor deposition (CVD) was first coated with a layer of polymethyl methacrylate (PMMA). Then, the PMMA-support MoS₂ (WSe₂) film was transferred to the WSe₂ (MoS₂) film on the PET flexible substrate in order to apply a uniaxial strain. The prepared heterostructures were immersed in acetone to remove PMMA, and vacuum annealing at 100 °C for 6 hours to eliminate residual polymer.³⁵

Steady-state characterizations

Steady-state absorption and PL spectra were characterized with Shimadzu UV-2550 and FL-4600, spectrophotometers, respectively. Raman spectra were measured by Alpha 300R, where the excitation wavelength of the laser was 532 nm and the spot size was approximately 0.5 mm for Raman measurements.

Femtosecond broadband TA system

We used a mode-locked Ti: sapphire amplifier to generate an 800 nm (repetition rate: 500 Hz) laser pulse with 35 fs pulse width (Solstice, Spectra-Physics). The system split the beam through an 80% (reflection)/20% (transmittance) mirror: one stronger beam of light passed through the TOPAS system to produce 750 nm excitation light; the other was through a 2 mm water, producing a broad-band probe light (400–800 nm). The signals of TA were gathered in a fiber-coupled spectrometer. The dispersion correction of TA data was performed by a chirp program.

Results and discussion

The two-point bending method shown in Fig. 1a imposes a uniaxial tensile strain on the samples.

The sample is clamped between two pairs of screw posts (SP). Thus, the tensile strain applied on samples is controlled by changing the distance (d) between two transition stages (TS). For example, when the d is reduced, the substrate is a bender, leading to a stronger uniaxial tensile strain applied on the substrate surface. Thus, this surface tension on the substrate will be transferred to the tightly attached samples on the surface of the substrate. The applied strain (ϵ) could be calculated with the formula: $\epsilon = l/R$, where l is the half-thickness of the substrate, R is the bending radius.¹⁴ In this work, we have applied 0%–1.2% uniaxial strains on the monolayer and heterostructure samples.

First, we measured Raman spectra of monolayer MoS₂ and WSe₂ under different strained conditions as shown in Fig. 1b and c, respectively. For the unstrained monolayer MoS₂, two characteristic peaks are E_{2g}¹ at 384 cm⁻¹ and A_{1g} at 403 cm⁻¹, corresponding to the in-plane vibration and out-of-plane vibrational modes, respectively.²⁸ As the applied strain increases, E_{2g}¹ and A_{1g} characteristic peaks of MoS₂ are red-shifted. This could be attributed to the phonon frequency softening induced by larger lattice constants.²⁸ The E_{2g}¹ peak of the CVD-grown monolayer TMDCs does not split like the mechanical exfoliated ones.^{14,27} To further illustrate the influence of tensile strain on phonon vibrational modes, we plot the Raman peak shifts as a function of strain changes, which present a linear relationship as reported previously (Fig. 1d).²⁷ The shifts of Raman peaks indicate that the strain indeed has been applied on TMDCs. It was estimated that, for MoS₂, redshifts were by a slope of -6.22 ± 0.62 cm⁻¹ per % strain and -4.75 ± 0.66 cm⁻¹ per % strain for E_{2g}¹ peak and A_{1g} peak, respectively. The monolayer WSe₂ has a similar phenomenon for Raman peak shifts under applied strains, where, its E_{2g}¹ peak is shifted by a slope of -3.75 ± 0.21 cm⁻¹ per % strain. The Raman spectra of MoS₂-WSe₂ heterostructure under applied strains are shown in Fig. S1,† where the E_{2g}¹ peak of WSe₂, E_{2g}¹ and A_{1g} peaks of MoS₂ redshifted by a slope of -0.45 ± 0.1 cm⁻¹ per % strain, -3.63 ± 0.65 cm⁻¹ per % strain, -1.50 ± 0.53 cm⁻¹ per % strain, respectively. The different shifts of Raman peaks between monolayer and heterostructure could be attributed to the strain-modulated interlayer interaction of the heterostructure.²⁷

Then, to directly investigate the strain effects on band structure evolution and exciton relaxation, we performed TA experiments on monolayer MoS₂ and WSe₂ materials under various tensile strains. The samples were excited by 400 nm pump pulses with a fluence of 6.5 μJ cm⁻². As the CVD-grown monolayer is a multicrystal material, the probing signals (within the detection spot with a diameter of ~0.3 mm) are average values for monolayer TMDCs with different crystal orientations and the resulting bilayer heterostructures with different twisting angles between the top and bottom layers. The negative signals around three excitonic absorption peaks in the TA spectra of MoS₂ (WSe₂) are known as the ground state bleaching (GSB) of each exciton state, which is due to state filling. The three initial GSB peaks probed at 0.3 ps for unstrained monolayer MoS₂ in Fig. 2a are located at 427 nm (2.904 eV), 603 nm (2.056 eV), and 649 nm (1.911 eV), corresponding to the C-exciton peak, B-exciton peak, and A-exciton peak,

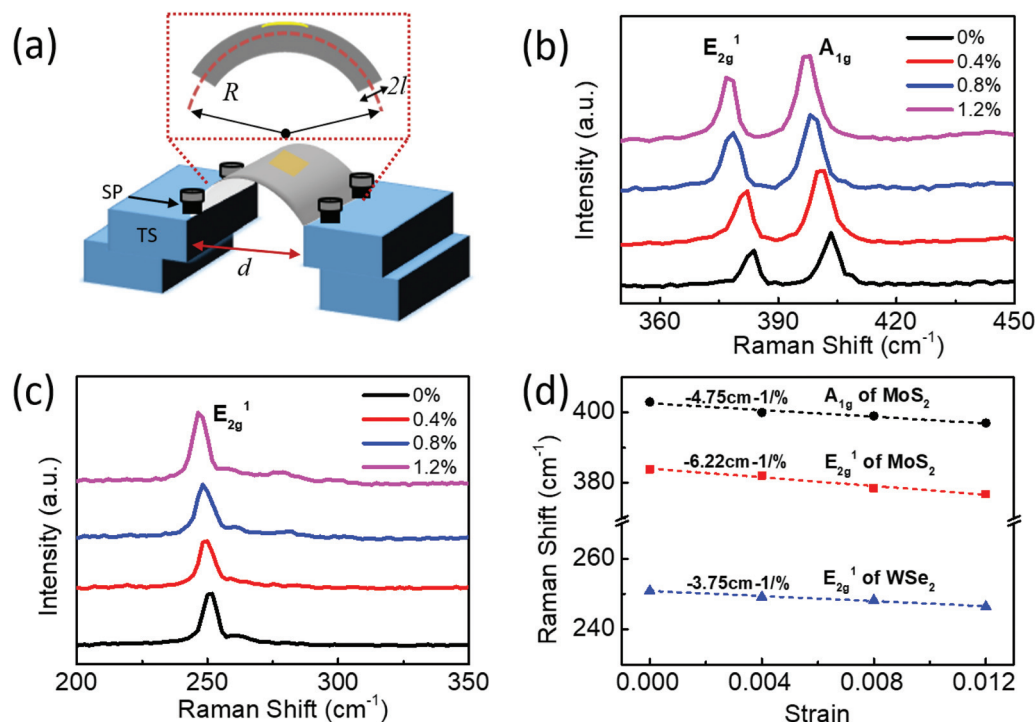


Fig. 1 (a) Schematic of the two-point bending apparatus and calculation principle to the applied strain. R , bending radius; l , half-thickness of the substrate; SP, screw posts; TS, transition stages; d , the distance between the two TSs. (b) Raman spectra of monolayer MoS₂ as the strain increases from 0% to 1.2%. (c) Raman spectra of monolayer WSe₂ as the strain increases from 0% to 1.2%. (d) Evolution of the E_{2g}¹ and A_{1g} peaks of monolayer MoS₂ and E_{2g}¹ peaks of monolayer WSe₂ as a function of applied tensile strains.

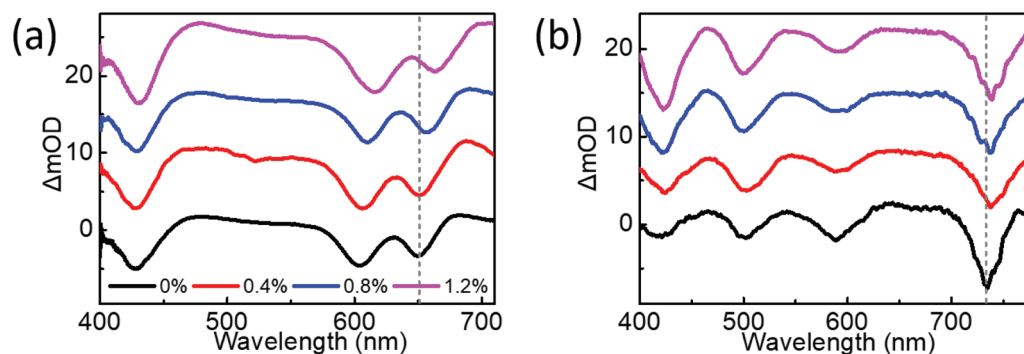


Fig. 2 Initial TA spectra for (a) monolayer MoS₂ and (b) WSe₂ probed at 0.3 ps under 0%–1.2% tensile strain (the pump wavelength is 400 nm).

respectively. The band-edge A- and B-excitons originate from the spin-orbit splitting at the bottom of the conduction band and at the top of the valence band for TMDCs, which are near the K valley; while the C exciton is a weak bound exciton, which is ascribed to inter-band transitions in the band-nesting zone between Γ and Q valleys in band structures.²⁹ The exciton dynamics of monolayer MoS₂ are shown in Fig. S2,† where the exciton relaxation process of C-excitons is significantly slower than A- and B-excitons.³⁰ The A-exciton peak of monolayer MoS₂ gradually redshifts as the applied strain increases (Fig. 2a). Under 1.2% uniaxial tensile strain, the A-exciton peak of MoS₂ redshifts from 649 nm (1.911 eV, unstrained case) to

663 nm (1.870 eV), indicating that the energy bandgap at K point shrinks about 41 meV. The B-exciton peak has a similar changing trend to that of A-exciton. However, the C-exciton peak does not shift obviously. The kinetics of B- and C-exciton remain unchanged under 0%–1.2% tensile strain, but it becomes faster with the increase of the strain for A-exciton (Fig. S2†). It should be pointed out that the TA signal of A-exciton is partially overlapping with that of the A-trion, so the kinetics change of A-exciton may be due to the different yield (or formation rate) of A-trions under the applied strains.³¹ For the unstrained monolayer WSe₂, its four initial GSB peaks are located at 420 nm (2.952 eV), 500 nm (2.480 eV),

590 nm (2.102 eV), 734 nm (1.689 eV), corresponding to C-, A⁻, B- and A-exciton peak, respectively.³² When the mechanical tensile strain is applied to monolayer WSe₂, the GSB peak of A-exciton of WSe₂ is red-shifted from 734 nm (1.689 eV, unstrained case) to 741 nm (1.673 eV) under 1.2% tensile strain, which means that the energy bandgap at K point shrinks by about 16 meV. Similar to the case of monolayer MoS₂, the exciton kinetics of monolayer WSe₂ also barely change under strains (Fig. S3[†]). In addition to the bandgap change, the evolution of the energy band can be further understood by comparing the ratio of the initial filling population of C-exciton (representing the Γ valley) to the sum of A-excitons and B-excitons (representing the K valley) for monolayer TMDCs.^{31,33} Under 1.2% tensile strain, the value of the ratio in monolayer MoS₂ (or WSe₂) increases from 0.62 (or 0.20) to 0.79 (or 1.07), which indicates a strain-induced band structure renormalization for monolayer TMDCs. All the values of the relative carrier population ratio under applied strains for monolayer MoS₂ and monolayer WSe₂ are summarized in Table S2,[†] which clearly indicate the effect of strain on the band structures of TMDCs. According to theoretical calculations, monolayer MoS₂ is a direct bandgap semiconductor, most of the photocarriers are distributed at the K valley.^{1,2} So, its band structure renormalization under applied strains is mainly determined by the location of the valence band maximum (VBM) at both the Γ and K valleys. That is, the local

VBM at Γ valley rises faster than that at K valley as the strain increases, which eventually makes the local VBM at Γ valley higher than that at K valley.¹⁴ As a result, monolayer MoS₂ becomes an indirect band semiconductor under applied strains, and the photo-generated carriers (it is mainly holes) will tend to relax into the Γ valley rather than staying at K-valley. This explains that the relative carrier population ratio of C/(A + B) increases with the larger strain, which means that there is a higher initial carrier population at the Γ valley, too. For monolayer WSe₂, since the local position of VBM at Γ valley increases faster than that at K valley, it even could accommodate more carriers than the case in monolayer MoS₂.^{23,34} Those observations in our TA experiments for monolayer MoS₂ and WSe₂ suggest that when the tensile strains are applied, the Γ valley of monolayer WSe₂ is more sensitive to that of monolayer MoS₂, while the K valley of monolayer MoS₂ is more sensitive to that of monolayer WSe₂.

At last, TA experiments for type-II MoS₂-WSe₂ heterostructures under various tensile strains are also carried out. Fig. S5[†] is the typical optical microscopic image for MoS₂-WSe₂ heterostructures where it clearly shows the superposition regions (triangular monolayer MoS₂ crystals are stacked on the quasi-continuous monolayer WSe₂ film). The steady-state absorption spectra for unstrained monolayer MoS₂, monolayer WSe₂, and MoS₂-WSe₂ heterostructures are presented in Fig. 3a. It shows a slight blue shift for both the A-exciton

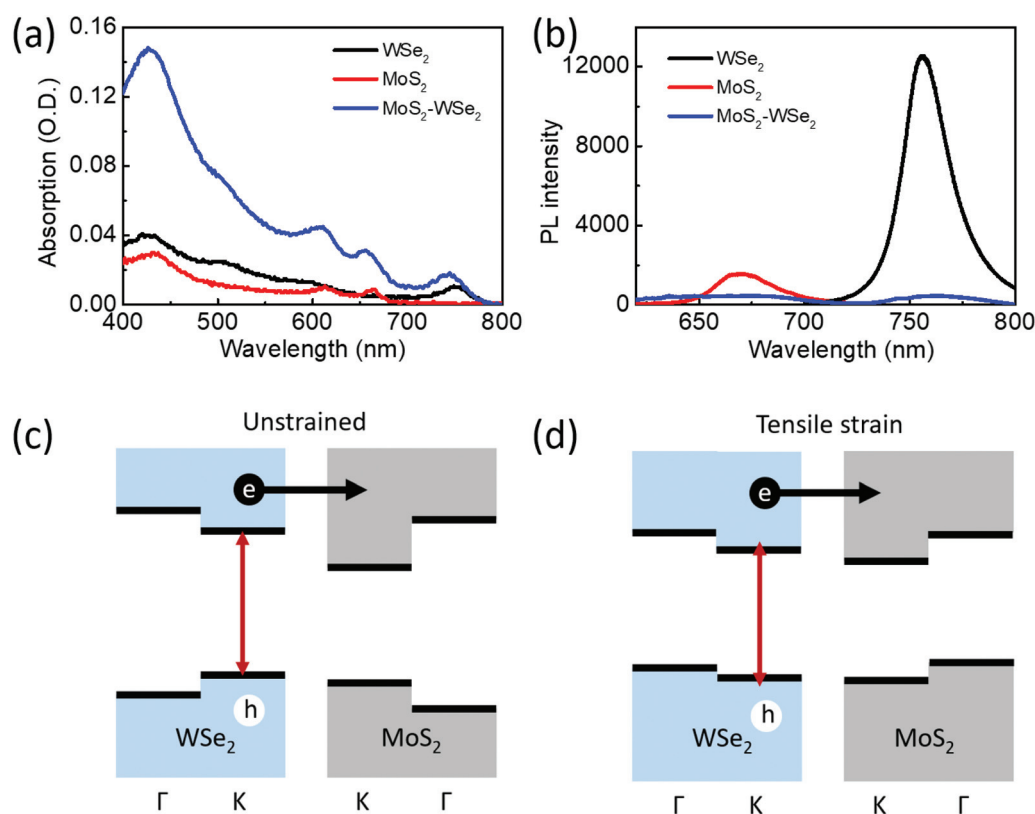


Fig. 3 (a) Steady-state absorption spectra for monolayer MoS₂, monolayer WSe₂ and MoS₂-WSe₂ heterostructures. (b) Steady-state PL spectra for MoS₂-WSe₂ heterostructures. Schematics of band alignment for MoS₂-WSe₂ heterostructures (c) without and (d) with tensile strains.

peaks of MoS₂ and WSe₂ in MoS₂-WSe₂ heterostructures, compared with the monolayer cases, implying an interlayer coupling of MoS₂-WSe₂ heterostructure. The fluorescence intensity of MoS₂-WSe₂ heterostructures is strongly quenched, too, compared with monolayer MoS₂ and WSe₂ (Fig. 3b), due to the charge transfer occurring at the interface.³⁵

The charge transfer rate of the donor and acceptor is closely related to the free energy ΔG in weak-coupling cases, according to the classical Marcus charge transfer theory, which could be regarded as the band offset between heterostructure to a certain degree.^{36,37} In our following case, we only considered the transfer of electrons from WSe₂ to MoS₂, when only WSe₂ is excited under 750 nm excitation. Since the relative position of the conduction band minimum (CBM) of WSe₂ is 0.76 eV higher than that of MoS₂,³⁸ and the conduction band of MoS₂ is almost unchanged under applied strains,¹⁴ while the conduction band of WSe₂ shifts down with strain increasing,^{23,34} resulting in a decreased ΔG for the band-edge charge transfer (Fig. 3c and d).

In order to directly observe the charge transfer process in MoS₂-WSe₂ heterostructures at room temperature, we tune the wavelength of excitation light to the band edge of WSe₂ (750 nm) with a pump fluence around 1.5 $\mu\text{J cm}^{-2}$ and choose the probe window near its band-edge region of monolayer MoS₂ and WSe₂, which avoids directly exciting MoS₂ because

the pump energy is far below the absorption energy threshold of MoS₂. As shown in Fig. 4a, there are three GSB peaks for the initial TA spectra of unstrained MoS₂-WSe₂ heterostructures located at 606 nm (2.046 eV), 654 nm (1.896 eV) and 742 nm (1.671 eV). There are only tiny differences from the peak positions of monolayers, which are caused by the interlayer coupling in MoS₂-WSe₂ heterostructures. When 1.2% tensile strain is applied to MoS₂-WSe₂ heterostructures, GSB peaks for A-exciton of MoS₂ and A-exciton of WSe₂ redshift to 663 nm (1.870 eV) and 753 nm (1.647 eV), respectively. Accordingly, the energy band at K point for MoS₂ layer and WSe₂ layer shrink about 26 meV and 24 meV, respectively, in MoS₂-WSe₂ heterostructure. All the estimated band shrinkage values at the K point under applied strains according to the red-shift of A-exciton peak for monolayer MoS₂, monolayer WSe₂ and MoS₂-WSe₂ heterostructure are summarized in Table S3.†

Interestingly, the A-exciton signal of MoS₂ occurs initially, indicating an effective charge transfer in MoS₂-WSe₂ heterostructures. Noting that the whole band structure of MoS₂-WSe₂ heterostructures generally changes under applied strains (especially, monolayer MoS₂ and WSe₂ have already changed from direct bandgap to indirect bandgap in those cases), the band-edge charge transfer in MoS₂-WSe₂ heterostructures is still available. One of the reasonable explanations could be that the rate of charge transfer is faster than momentum-mis-

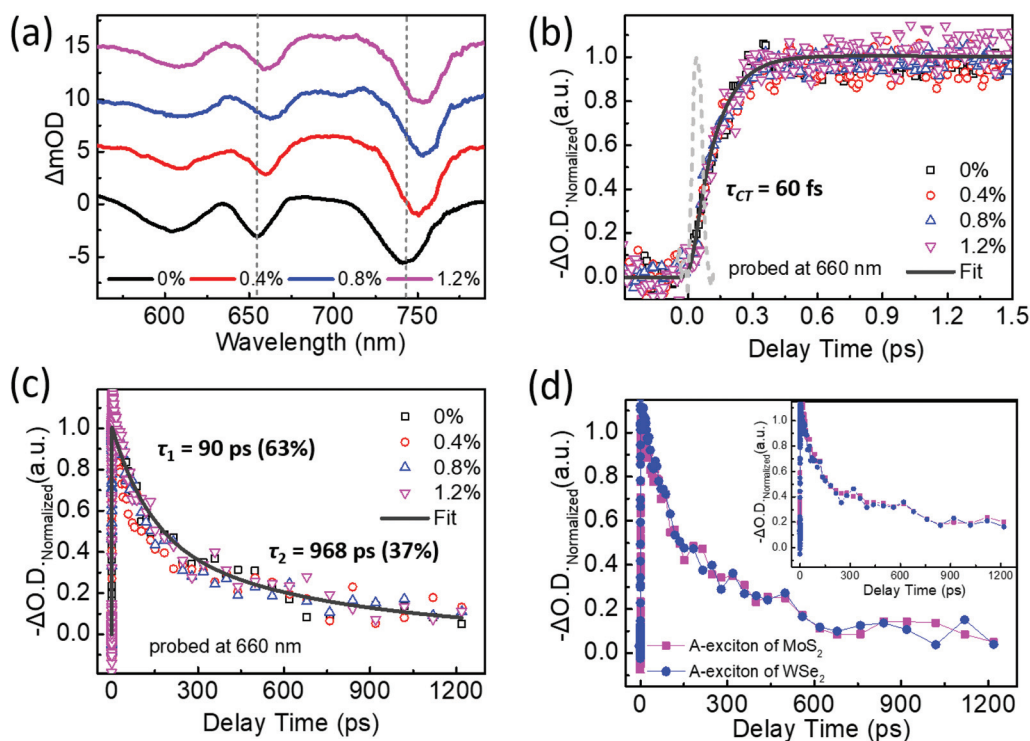


Fig. 4 (a) Initial TA spectra for 0%–1.2% strained MoS₂-WSe₂ heterostructures probed at 1 ps (the pump wavelength is 750 nm). (b) Charge transfer process of MoS₂-WSe₂ heterostructure excited by the 750 nm pulses under 0%–1.2% strain probed at 660 nm. (c) Charge recombination processes represented by the A-exciton dynamics of MoS₂ in MoS₂-WSe₂ heterostructures excited by the 750 nm pulses under 0%–1.2% strain probed at 660 nm. (d) Renormalized charge recombination dynamics of MoS₂-WSe₂ without strain probed at 660 nm (pink solid square) and 740 nm (blue solid circle). The inset shows the renormalized charge recombination dynamics of MoS₂-WSe₂ under a 1.2% strain. The dashed line in (b) is the instrument response function (IRF).

matched intervalley scattering. So that, charge transfer is almost unaffected under strain. The quantum coherence and donor–acceptor delocalization also may be contributing to this interfacial charge transfer in van der Waals junctions.³⁹ Fig. 4b shows the charge transfer processes of MoS₂-WSe₂ heterostructures under different tensile strains, which are surprisingly the same as those in the unstrained cases. In other words, the rate of charge transfer is robust under applied tensile strains in our experimental range. After the deconvolution treatment, we obtained the robust charge transfer time in MoS₂-WSe₂ heterostructures is around 60 ± 4 fs. In addition, the driving force change for MoS₂-WSe₂ heterostructures is on the order of a few tens of meV here, comparable to the kT energy. It implies that the changing trend of the charge transfer rate as a function of the driving force could be relatively flat in such a small variation range, which could be one of the reasons for the observed robust interfacial charge transfer in MoS₂-WSe₂ heterostructures.

Those experimental results demonstrate that, unlike classical charge transfer systems, even band structure (driving force) tuning by applied strains has little impact on the band-edge charge transfer rate of TMDC heterostructures. It has been testified that the robust band-edge charge transfer rate in TMDC heterostructures could be independent of dielectric environment, temperature, and twist angle.^{40–42} Recently, it has been further reported that the band-edge charge transfer in TMDC heterostructures could be manipulated by the thickness of each component,^{43,44} which are explained by the dielectric environment changing induced modification for the effective interaction distance in TMDC heterostructures. Besides, the band-edge charge transfer rate could be tuned by interlayer coupling, which is successfully depicted by the quantum tunneling model.⁴⁵ Nowadays, the charge transfer mechanism in TMDC heterostructures is still controversial and requires further theoretical calculations to be fully understood.

For the charge recombination processes, the GSB recovering of A-excitons of MoS₂ (probe at 660 nm) and WSe₂ (probe at 740 nm) reflect the decay of electrons and holes, respectively. As one can see in Fig. 4c, the dynamics of the electrons are also robust under 0%–1.2% tensile strains. Furthermore, at longer probe times (≥ 30 ps), the decay of holes follows the same kinetics as that of the electrons, in both unstrained and applied strain (such as 1.2% strain) cases (Fig. 4d). This simultaneous decay of the electrons in the MoS₂-layer and holes in the WSe₂-layer clearly indicates the formation of tightly bound interlayer excitons, which is responsible for the following recombination of separated charges in MoS₂-WSe₂ heterostructures, when only monolayer WSe₂ is excited.⁴⁶ Their kinetics could be well fitted by a biexponential decay, which gives the interlayer electron-hole recombination time constants as 90 ± 8 ps (63%) and 968 ± 190 ps (37%). The biexponential decay processes could be due to the defect-assisted recombination.^{47,48} The above experimental results imply that when uniaxial tensile strains are applied to MoS₂-WSe₂ heterostructures, the band structure has little impact on the interlayer exciton recombination.²⁶

Conclusions

We systemically investigated the strain-mediated band structure evolution for monolayer MoS₂ and monolayer WSe₂ and found robust band-edge charge transfer in MoS₂-WSe₂ heterostructures by Raman spectroscopy and femtosecond transient absorption spectroscopy. The shifts of the Raman peak and the changes of relative carrier population ratio in Γ and K valleys from TA results for the above monolayer TMDCs clearly indicate that the strains have been applied, and the strain effects change the relative positions of valleys in band structures, respectively. When the mechanical tensile strain applied to monolayer MoS₂ (WSe₂) increases from 0% to 1.2%, the bandgap at the K point shrinks 41 meV and 16 meV for tensile strained monolayer MoS₂ and WSe₂, respectively, according to the redshift of A-exciton bleaching peak in TA experiments. Those results demonstrate that Γ and K valleys in monolayer WSe₂ and monolayer MoS₂ have different strain responses. Furthermore, due to the mismatched strain response for the excitons in monolayer MoS₂ and WSe₂, the bandgaps at K point for MoS₂ and WSe₂ in the MoS₂-WSe₂ heterostructure shrink about 26 meV and 24 meV, respectively. It is found that the resulting band offset change for MoS₂-WSe₂ heterostructures under a tensile strain would not affect the band-edge electron transfer processes, where only monolayer WSe₂ is excited. From an optoelectronic applications perspective, robust charge transfer under strain engineering in TMDC heterostructures is very advantageous to maintain the performance of flexible devices based on monolayer TMDCs and their composites in winding circumstances.

Author contributions

The manuscript was written through the contributions of all authors. All authors have given approval to the final version of the manuscript.

Conflicts of interest

There are no conflicts to declare.

Acknowledgements

This work was supported by the National Key Research and Development Program of China and the National Natural Science Foundation of China (NSFC) under Grants 2017YFB1104300, 21773087, 21603083, 61927814, and 21903035.

References

- 1 K. F. Mak, C. Lee, J. Hone, J. Shan and T. F. Heinz, *Phys. Rev. Lett.*, 2010, **105**, 136805.

- 2 A. Splendiani, L. Sun, Y. Zhang, T. Li, J. Kim, C. Y. Chim, G. Galli and F. Wang, *Nano Lett.*, 2010, **10**, 1271–1275.
- 3 A. M. Jones, H. Yu, N. J. Ghimire, S. Wu, G. Aivazian, J. S. Ross, B. Zhao, J. Yan, D. G. Mandrus, D. Xiao, W. Yao and X. Xu, *Nat. Nanotechnol.*, 2013, **8**, 634–638.
- 4 J. Wang, H. Li, Y. Ma, M. Zhao, W. Liu, B. Wang, S. Wu, X. Liu, L. Shi, T. Jiang and J. Zi, *Light: Sci. Appl.*, 2020, **9**, 148.
- 5 C. Mai, A. Barrette, Y. Yu, Y. G. Semenov, K. W. Kim, L. Cao and K. Gundogdu, *Nano Lett.*, 2014, **14**, 202–206.
- 6 J. Wang, Q. Yao, C. W. Huang, X. Zou, L. Liao, S. Chen, Z. Fan, K. Zhang, W. Wu, X. Xiao, C. Jiang and W. W. Wu, *Adv. Mater.*, 2016, **28**, 8302–8308.
- 7 H. Wang, H. Y. Wang, Q. D. Chen, H. L. Xu, H. B. Sun, F. Huang, W. Raja, A. Toma and R. Proietti Zaccaria, *Laser Photonics Rev.*, 2018, **12**, 1700176.
- 8 P. Zhang, C. Bian, J. Ye, N. Cheng, X. Wang, H. Jiang, Y. Wei, Y. Zhang, Y. Du, L. Bao, W. Hu and Y. Gong, *Sci. China Mater.*, 2020, **63**, 1548–1559.
- 9 H. Lin, Z. Q. Xu, G. Cao, Y. Zhang, J. Zhou, Z. Wang, Z. Wan, Z. Liu, K. P. Loh, C. W. Qiu, Q. Bao and B. Jia, *Light: Sci. Appl.*, 2020, **9**, 137.
- 10 G. Kakavelakis, I. Paradisanos, B. Paci, A. Generosi, M. Papachatzakis, T. Maksudov, L. Najafi, A. E. Del Rio Castillo, G. Kioseoglou, E. Stratakis, F. Bonaccorso and E. Kymakis, *Adv. Energy Mater.*, 2018, **8**, 1702287.
- 11 S. Manzeli, D. Ovchinnikov, D. Pasquier, O. V. Yazyev and A. Kis, *Nat. Rev. Mater.*, 2017, **2**, 17088.
- 12 T. Shen, A. V. Penumatcha and J. Appenzeller, *ACS Nano*, 2016, **10**, 4712–4718.
- 13 C. Si, Z. Sun and F. Liu, *Nanoscale*, 2016, **8**, 3207–3217.
- 14 H. J. Conley, B. Wang, J. I. Ziegler, R. F. Haglund Jr., S. T. Pantelides and K. I. Bolotin, *Nano Lett.*, 2013, **13**, 3626–3630.
- 15 E. Singh, P. Singh, K. S. Kim, G. Y. Yeom and H. S. Nalwa, *ACS Appl. Mater. Interfaces*, 2019, **11**, 11061–11105.
- 16 D. Yin, N. R. Jiang, Y. F. Liu, X. L. Zhang, A. W. Li, J. Feng and H. B. Sun, *Light: Sci. Appl.*, 2018, **7**, 35.
- 17 P. Lin, L. Zhu, D. Li, L. Xu, C. Pan and Z. Wang, *Adv. Funct. Mater.*, 2018, **28**, 1802849.
- 18 J. Du, H. Yu, B. Liu, M. Hong, Q. Liao, Z. Zhang and Y. Zhang, *Small Methods*, 2021, **5**, 2000919.
- 19 L. Dong, R. R. Namburu, T. P. O'Regan, M. Dubey and A. M. Dongare, *J. Mater. Sci.*, 2014, **49**, 6762–6771.
- 20 I. Niehues, R. Schmidt, M. Druppel, P. Marauhn, D. Christiansen, M. Selig, G. Berghauser, D. Wigger, R. Schneider, L. Braasch, R. Koch, A. Castellanos-Gomez, T. Kuhn, A. Knorr, E. Malic, M. Rohlfing, S. Michaelis de Vasconcellos and R. Bratschitsch, *Nano Lett.*, 2018, **18**, 1751–1757.
- 21 S. Bhattacharyya, T. Pandey and A. K. Singh, *Nanotechnology*, 2014, **25**, 465701.
- 22 R. Rosati, S. Brem, R. Perea-Causin, R. Schmidt, I. Niehues, S. Michaelis de Vasconcellos, R. Bratschitsch and E. Malic, *2D Mater.*, 2020, **8**, 015030.
- 23 S. B. Desai, G. Seol, J. S. Kang, H. Fang, C. Battaglia, R. Kapadia, J. W. Ager, J. Guo and A. Javey, *Nano Lett.*, 2014, **14**, 4592–4597.
- 24 J. Priya and V. B. Shenoy, *ACS Nano*, 2012, **6**, 5449–5456.
- 25 A. Kumar and P. K. Ahluwalia, *Physica. B*, 2013, **419**, 66–75.
- 26 Y. Yang, W. H. Fang, A. Benderskii, R. Long and O. V. Prezhdo, *J. Phys. Chem. Lett.*, 2019, **10**, 7732–7739.
- 27 S. Pak, J. Lee, Y. W. Lee, A. R. Jang, S. Ahn, K. Y. Ma, Y. Cho, J. Hong, S. Lee, H. Y. Jeong, H. Im, H. S. Shin, S. M. Morris, S. Cha, J. I. Sohn and J. M. Kim, *Nano Lett.*, 2017, **17**, 5634–5640.
- 28 C. Lee, H. Yan, L. E. Brus, T. F. Heinz, J. Hone and S. Ryu, *ACS Nano*, 2010, **4**, 2695–2700.
- 29 A. Steinhoff, J. H. Kim, F. Jahnke, M. Rosner, D. S. Kim, C. Lee, G. H. Han, M. S. Jeong, T. O. Wehling and C. Gies, *Nano Lett.*, 2015, **15**, 6841–6847.
- 30 L. Wang, Z. Wang, H. Y. Wang, G. Grinblat, Y. L. Huang, D. Wang, X. H. Ye, X. B. Li, Q. Bao, A. S. Wee, S. A. Maier, Q. D. Chen, M. L. Zhong, C. W. Qiu and H. B. Sun, *Nat. Commun.*, 2017, **8**, 13906.
- 31 K. F. Mak, K. He, C. Lee, G. H. Lee, J. Hone, T. F. Heinz and J. Shan, *Nat. Mater.*, 2013, **12**, 207–211.
- 32 X. Chen, Z. Wang, L. Wang, H. Y. Wang, Y. Y. Yue, H. Wang, X. P. Wang, A. T. S. Wee, C. W. Qiu and H. B. Sun, *Nanoscale*, 2018, **10**, 9346–9352.
- 33 Y. Y. Yue, Z. Wang, L. Wang, H. Y. Wang, Y. Chen, D. Wang, Q. D. Chen, B. R. Gao, A. T. S. Wee, C. W. Qiu and H. B. Sun, *Nanotechnology*, 2021, **32**, 135208.
- 34 W. T. Hsu, L. S. Lu, D. Wang, J. K. Huang, M. Y. Li, T. R. Chang, Y. C. Chou, Z. Y. Juang, H. T. Jeng, L. J. Li and W. H. Chang, *Nat. Commun.*, 2017, **8**, 929.
- 35 X. Hong, J. Kim, S. F. Shi, Y. Zhang, C. Jin, Y. Sun, S. Tongay, J. Wu, Y. Zhang and F. Wang, *Nat. Nanotechnol.*, 2014, **9**, 682–686.
- 36 R. A. Marcus, *J. Chem. Phys.*, 1956, **24**, 966.
- 37 L. Wang, H.-Y. Wang, H.-T. Wei, H. Zhang, Q.-D. Chen, H.-L. Xu, W. Han, B. Yang and H.-B. Sun, *Adv. Energy Mater.*, 2014, **4**, 1308812.
- 38 M. H. Chiu, C. Zhang, H. W. Shiu, C. P. Chuu, C. H. Chen, C. Y. Chang, C. H. Chen, M. Y. Chou, C. K. Shih and L. J. Li, *Nat. Commun.*, 2015, **6**, 7666.
- 39 R. Long and O. V. Prezhdo, *Nano Lett.*, 2016, **16**, 1996–2003.
- 40 H. Zhu, J. Wang, Z. Gong, Y. D. Kim, J. Hone and X. Y. Zhu, *Nano Lett.*, 2017, **17**, 3591–3598.
- 41 H. Zhou, Y. Zhao and H. Zhu, *J. Phys. Chem. Lett.*, 2019, **10**, 150–155.
- 42 Z. Ji, H. Hong, J. Zhang, Q. Zhang, W. Huang, T. Cao, R. Qiao, C. Liu, J. Liang, C. Jin, L. Jiao, K. Shi, S. Meng and K. Liu, *ACS Nano*, 2017, **11**, 12020–12026.
- 43 S. W. Zheng, H. Y. Wang, L. Wang, H. Wang and H. B. Sun, *J. Phys. Chem. Lett.*, 2020, **11**, 9649–9655.
- 44 T. Zheng, P. Valencia-Acuna, P. Zereshki, K. M. Beech, L. Deng, Z. Ni and H. Zhao, *ACS Appl. Mater. Interfaces*, 2021, **13**, 6489–6495.
- 45 H. Zhou, Y. Zhao, W. Tao, Y. Li, Q. Zhou and H. Zhu, *ACS Nano*, 2020, **14**, 4618–4625.

- 46 Z. L. Wang, P. Altmann, C. Gadermaier, Y. T. Yang, W. Li, L. Ghirardini, C. Trovatiello, M. Finazzi, L. Duò, M. Celebrano, R. Long, D. Akinwande, O. V. Prezhdo, G. Cerullo and S. Dal Conte, *Nano Lett.*, 2021, **21**, 2165–2173.
- 47 H. Chen, X. Wen, J. Zhang, T. Wu, Y. Gong, X. Zhang, J. Yuan, C. Yi, J. Lou, P. M. Ajayan, W. Zhuang, G. Zhang and J. Zheng, *Nat. Commun.*, 2016, **7**, 12512.
- 48 H. Wang, C. Zhang and F. Rana, *Nano Lett.*, 2015, **15**, 339–345.